ELSEVIER

A lattice Boltzmann front-tracking method for interface dynamics with surface tension in two dimensions

Pierre Lallemand [a], Li-Shi Luo [b,*], Yan Peng [b]

[a] *LIMSI, Bâtiment 508, Université Paris-Sud (Paris XI Orsay), 91405 Orsay Cedex, France*
[b] *Department of Mathematics and Statistics, Old Dominion University, Norfolk, VA 23529, USA*

Abstract

We propose to combine the lattice Boltzmann equation (LBE) and the front-tracking (FT) method to simulate interfacial dynamics with surface tension in two dimensions (2D). In the proposed LBE-FT method, the flow is modeled by the LBE on a fixed Cartesian mesh, whereas interfaces are explicitly tracked by a set of markers that are advected by the flow. The interface curvature is computed from adjacent markers and is then used to determine surface tension according to Laplace's law. The local capillary forces evaluated at the markers are distributed to nearby Eulerian grid points according to a "smearing" function to approximate the Dirac delta function due to Peskin. To validate the proposed LBE-FT method, we simulate (1) a circular bubble in a flow either quiescent or moving with a constant velocity and (2) the decaying capillary waves at the interface of two fluids of equal viscosities and densities. For the circular bubble, the spurious current measured in the LBE-FT is weaker than that observed in the standard volume of fluid method and some existing LBE models. For the capillary waves, the numerical results of the period T (or frequency ω), the attenuation rate γ, the surface tension σ and the root-mean-square error of the wave amplitude agree well with the normal-mode and Prosperetti's solutions. The proposed LBE-FT method is shown to have a second-order rate of convergence. We also show that the LBE-FT method is superior to the existing lattice BGK diffusive interface method in terms of accuracy of interface representation, numerical stability and computational efficiency.
© 2007 Elsevier Inc. All rights reserved.

1. Introduction

In the recent decade there has been significant development in numerical methods for modeling and simulation of interface dynamics (cf. [1]). In particular, the front-tracking technique has emerged as a superior method [2–8]. Systematic comparisons show that front-tracking (FT) method is superior to particle methods,

---

* Corresponding author. Tel.: +1 757 683 5295; fax: +1 757 683 3885.
  E-mail addresses: lalleman@asci.fr (P. Lallemand), lluo@odu.edu (L.-S. Luo), ypeng@odu.edu (Y. Peng).
  URLs: http://www.lions.odu.edu/~lluo (L.-S. Luo), http://www.lions.odu.edu/~ypeng (Y. Peng).

PLIC-VOF, level sets and capturing, in that order [8,9]. The front-tracking method uses a set of discrete marker points connected to each other to form a piecewise linear (in 2D) or a triangular (in 3D) description of the interface. The marker points (or markers) are completely independent of the grid system upon which flow fields are computed, and are evolved in a Lagrangian manner.

In this paper we propose to combine the lattice Boltzmann equation (LBE) [10–12], an Eulerian method with a fixed Cartesian mesh, and the front-tracking method, a Lagrangian method with a set of marker points precisely representing interface positions, to model the interfacial dynamics with surface tension in two dimensions (2D). We note that there already existed other hybrid methods which couple the front-tracking technique with various CFD methods (e.g. [13,14]). Most existing LBE models for interface dynamics are diffusive interface capturing methods, which employ various "interactions" to produce interfaces with a thickness of a few lattice spacings [15,16]. In contrast, in the LBE front-tracking method proposed in this work, the coupling between the flow and markers is through the localized forces proportional to the interfacial curvature. In particular, the proposed LBE-FT method uses the immersed boundary method (IBM) due to Peskin [17,18] to treat the interface between two fluids. In IBM, the fluid variables are Eulerian ones discretized on a fixed Cartesian mesh, while the interfacial and other boundary conditions are carried by Lagrangian variables. The two types of variables are coupled by interaction equations involving a smoothed approximation of the Dirac delta function. The Eulerian-Lagrangian identities govern the transfer of data from one mesh to the other. Previously the IBM has been used in the LBE to treat fluid–solid interfaces [19].

As we will show in details later, the proposed LBE front-tracking method has several attractive features when compared to the existing multiphase LBE diffusive interface capturing method. First of all, the interfacial position is precisely defined by a set of markers, as opposed to by arbitrary contours of some continuous function. The precise interface representation is particularly useful to define initial conditions in the LBE simulations. Second, the LBE-FT method improves the numerical stability because of the multiple-relaxation-time collision model [20–23]. And third, the LBE-FT method enhances the computational efficiency. We would like to note that the LBE-FT method achieves these improvements while maintaining the algorithmic simplicity of the LBE method. The proposed LBE-FT method also shows the feasibility of incorporating sophisticated numerical techniques, such as the multigrid method, into the LBE method. These features of the proposed LBE-FT method will be demonstrated through numerical simulations.

The remainder of this paper is organized as follows. Section 2 provides a brief discussion of the LBE method and the front-tracking techniques, including dynamics of markers, determination of curvature and approximation made to distribute localized surface-tension forces to the fluid. Section 3 presents numerical results for two test cases in two dimensions: (a) a single bubble in a flow either quiescent or moving with a constant velocity and (b) the decaying capillary waves at the interface between two fluids of equal viscosities and densities. We also provide a comparison between the proposed LBE-FT method and an existing multiphase lattice BGK diffusive interface capturing method. Section 4 concludes the paper.

2. Numerical methods

In this section we will provide concise descriptions of the lattice Boltzmann equation with multiple-relaxation-time collision model [20–23] and the front-tracking method [17,18]. More detailed treatments of these methods can be found in pertinent literature.

2.1. Lattice Boltzmann equation

The lattice Boltzmann equation (LBE) is a simple explicit algorithm associated with a square or cubic lattice on which fictitious particles move synchronously from one grid point to one of its neighbors according to their (discrete) velocities. In the two dimensional (2D) case considered here, we will use the nine-velocity model on a square lattice (the D2Q9 model). On each grid point r_j of the model, there are nine real numbers $\{f_i | i = 0, 1, \ldots, 8\}$ representing the single-particle (mass) density distribution functions corresponding to the nine discrete particle velocities $\{c_i | i = 0, 1, \ldots, 8\}$. The discrete velocity set $\{c_i\}$ is depicted in Fig. 1. In the LBE method, the grid size δ_x, which is also the lattice constant of the square lattice, and the time step δ_t are chosen in such a way that "particles" advect in one time step from one grid point to an adjacent one
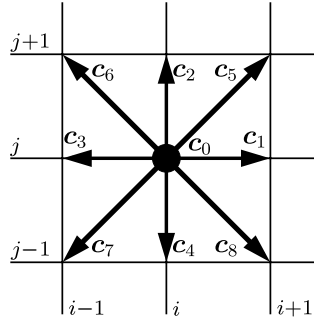
Fig. 1. Illustration of nine-velocity discretization in two dimensions resulting in exact advection to all immediate neighboring grid points on a regular Cartesian grid lattice with coordinates (i, j).

according to their velocities, as illustrated in Fig. 1. The evolution equation for the distribution functions $\{f_i\}$ can be written as follows:

$$\mathbf{f}(\mathbf{r}_j + \mathbf{c}\delta_t, t_n + \delta_t) = \mathbf{f}(\mathbf{r}_j, t_n) + \mathbf{\Omega}[\mathbf{f}(\mathbf{r}_j, t_n), \mathbf{F}(\mathbf{r}_j, t_n)], \tag{1}$$

where $\mathbf{\Omega}$ represents the collision operator in the presence of a space-dependent body force $\mathbf{F}$ and the bold-font symbols denote Q-tuple vectors, with Q being the number of the discrete velocities

$$\mathbf{f}(\mathbf{r}_j + \mathbf{c}\delta_t, t_n + \delta_t) = (f_0(\mathbf{r}_j, t_n + \delta_t), \ldots, f_8(\mathbf{r}_j + \mathbf{c}_8\delta_t, t_n + \delta_t))^\mathsf{T},$$
$$\mathbf{f}(\mathbf{r}_j, t_n) = (f_0(\mathbf{r}_j, t_n), f_1(\mathbf{r}_j, t_n), \ldots, f_8(\mathbf{r}_j, t_n))^\mathsf{T},$$
$$\mathbf{\Omega} = (\Omega_0(\mathbf{r}_j, t_n), \Omega_1(\mathbf{r}_j, t_n), \ldots, \Omega_8(\mathbf{r}_j, t_n))^\mathsf{T},$$

where T denotes the transpose operator.

The collision operator in the LBE method is modeled by the linear relaxation process, which is carried out in the moment space [20]

$$\mathbf{\Omega} = -\mathsf{M}^{-1} \cdot \mathsf{S} \cdot [\mathbf{m} - \mathbf{m}^{(\mathrm{eq})}], \tag{2}$$

where $\mathbf{m}$ and $\mathbf{m}^{(\mathrm{eq})}$ are moments and their equilibria, respectively, S is a positive-definite diagonal matrix of relaxation rates $\{s_i | i = 1, 2, \ldots, 9\}$

$$\mathsf{S} = \mathrm{diag}(s_1, s_2, \ldots, s_9),$$

and M is the transformation matrix mapping the distribution functions to their moments

$$\mathbf{m} = \mathsf{M} \cdot \mathbf{f}, \quad \mathbf{f} = \mathsf{M}^{-1} \cdot \mathbf{m}.$$

The equilibria of the moments are given by

$$m_1^{(\mathrm{eq})} = \delta\rho, \quad m_2^{(\mathrm{eq})} = -2\delta\rho + 3\mathbf{j} \cdot \mathbf{j}, \quad m_3^{(\mathrm{eq})} = \delta\rho - 3\mathbf{j} \cdot \mathbf{j}, \tag{3a}$$

$$m_4^{(\mathrm{eq})} = j_x, \quad m_5^{(\mathrm{eq})} = -j_x, \quad m_6^{(\mathrm{eq})} = j_y, \quad m_7^{(\mathrm{eq})} = -j_y, \tag{3b}$$

$$m_8^{(\mathrm{eq})} = j_x^2 - j_y^2, \quad m_9^{(\mathrm{eq})} = j_x j_y, \tag{3c}$$

where $\delta\rho$ is the density fluctuation, and $\mathbf{j} = (j_x, j_y)$ is the flow momentum, and they are the conserved moments of the distribution functions

$$\delta\rho = \sum_i f_i, \quad \mathbf{j} = \sum_i \mathbf{c}_i f_i = \rho_0 \mathbf{u}. \tag{4}$$

The total density is $\rho = \rho_0 + \delta\rho$, and the mean density ρ_0 is set to unity. Here we also use the incompressible approximation so that $\mathbf{j} \approx \rho_0 \mathbf{u} = \mathbf{u}$ [21,24], with $\rho_0 = 1$.

In the presence of a body force $\mathbf{F}$, the above collision operator is modified to include the acceleration of the fluid due to the body force $\mathbf{F}$. In practice [23,25,26], the LBE algorithm is decomposed in the following steps:

- Compute moments $\mathbf{m} = \mathsf{M} \cdot \mathbf{f}$;
- Compute $\mathbf{j}' = \mathbf{j} + \mathbf{F}\delta_t/2$, $\mathbf{j}'$ is used to advect the markers and as the output of the flow momentum;
- Use $\mathbf{j}'$ to compute the equilibria of Eqs. (3), then relax the non-conserved moments;
- Compute $\mathbf{j}'' = \mathbf{j}' + \mathbf{F}\delta_t/2$;
- Compute the post-collision distribution $\mathbf{f}^*$ with $\mathbf{j}''$ as the momentum;
- Advect $\mathbf{f}^*$.

The lattice Boltzmann equation approximates the incompressible Navier–Stokes equation with second-order spatial accuracy (e.g. [27]). The kinematic and bulk viscosities of the model are

$$v = \frac{1}{3}\left(\frac{1}{s_8} - \frac{1}{2}\right)c\delta_x, \quad \zeta = \frac{1}{6}\left(\frac{1}{s_2} - \frac{1}{2}\right)c\delta_x, \quad c = \frac{\delta_x}{\delta_t}. \tag{5}$$

The speed of sound in the model is

$$c_s = \frac{1}{\sqrt{3}}c. \tag{6}$$

The LBE method with the polynomial equilibria for the non-conserved moments is only valid in the near incompressible limit, i.e., the Mach number $Ma = U/c_s \ll 1$. In practice, $Ma < 0.3$. Further details of the MRT LBE can be found in, for example, [20–23].

2.2. Front-tracking technique

We will use front-tracking technique to track fluid–fluid interfaces. Again, we shall restrict ourselves in 2D here. Suppose an interface between fluids I and II is represented by a curve, which is discretized into a number of points (markers) with coordinates $\{\mathbf{x}_k | k = 1, 2, \ldots, N\}$, as illustrated in Fig. 2. These marker points are connected to one another to form a piecewise linear description of the interface in 2D. This can be generalized to 3D where the markers points are connected to form a triangulation of the interface. The Lagrangian dynamics of the markers due to advection by the fluid flow is carried out as follows. At each iteration of the algorithm, the LBE method determines the velocity field $\mathbf{u}$ and the pressure field p at the grid points $\{\mathbf{r}_j\}$ on the fixed Cartesian mesh $\delta_x \mathbb{Z}^d$. The velocity $\mathbf{u}$ at each marker point can be obtained by interpolations involving nearby grid points, and the markers are advected according to the explicit forward Eulerian advection

$$\mathbf{x}_k(t_n + \delta_t) = \mathbf{x}_k(t_n) + \mathbf{u}(\mathbf{x}_k, t_n)\delta_t. \tag{7}$$

After this Lagrangian step for the markers, markers may be added or deleted to maintain the distance between two adjacent markers $\ell_{kl} = |\mathbf{x}_k - \mathbf{x}_l|$ in a reasonable length ℓ_0 in terms of the grid spacing δ_x. Typically in our numerical computations, if $\ell_{kl} > 1.1\ell_0$, a new marker is added between $\mathbf{x}_k$ and $\mathbf{x}_l$, whereas if $\ell_{kl} < 0.5\ell_0$, either $\mathbf{x}_k$ or $\mathbf{x}_l$ is to be eliminated. This is easy to carry out unless topological changes of the interface occur. Note that the simple Eulerian dynamics in Eq. (7) could easily be modified to improve accuracy in time or to include
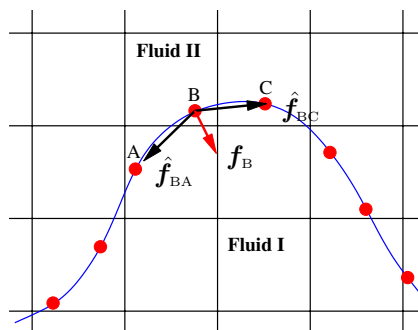

Fig. 2. Illustration of interface (the curve) and markers (dots) and the square grid for D2Q9 model.

other properties of the interface, such as interface rigidity, interface viscosity or interaction of the interface with external fields.

The local curvature is a relevant quantity for modeling of the surface tension σ. The curvature $C = 1/R$ at point B is proportional to $|\boldsymbol{f}_B| = |\hat{\boldsymbol{f}}_{BA} + \hat{\boldsymbol{f}}_{BC}|$ weighted by the mean distance $\bar{\ell}_B = \frac{1}{2}(\ell_{BA} + \ell_{BC})$, where $\hat{\boldsymbol{f}}_{BA}$ and $\hat{\boldsymbol{f}}_{BC}$ are unit vectors along $\overline{BA}$ and $\overline{BC}$, respectively, as illustrated in Fig. 2. Thus, the local body force due to the surface tension σ at point B is given by

$$\boldsymbol{f}(\boldsymbol{r}_B) = \sigma \bar{\ell}_B \boldsymbol{f}_B, \quad \boldsymbol{f}_B = \hat{\boldsymbol{f}}_{BA} + \hat{\boldsymbol{f}}_{BC}. \tag{8}$$

Because the markers usually do not reside on grid points, the forces computed at the marker positions must be distributed to the nearby grid points somehow. Here a scheme proposed by Peskin [17] is used to distribute the capillary forces. For instance, at the point $\boldsymbol{x}_B = (x_B, y_B)$, the weight to distribute force $\boldsymbol{f}(\boldsymbol{x}_B)$, to a nearby grid point $\boldsymbol{r}_j = (x_j, y_j)$ is given by $W(\boldsymbol{r}_j) = w(x_j, i_B)w(y_j, j_B)$ and

$$w(x_j, i_B) = \begin{cases} \frac{1}{2n}\{1 + \cos[(x_j/\delta_x - i_B)\pi/n]\}, & |x_j/\delta_x - i_B| \leqslant n, \\ 0, & |x_j/\delta_x - i_B| > n, \end{cases} \tag{9}$$

where i_B and j_B are integers closest to x_B/δ_x and y_B/δ_x, respectively. That is, the force $\boldsymbol{f}(\boldsymbol{r}_B)$ evaluated at the marker point B with coordinates $\boldsymbol{x}_B = (x_B, y_B)$ is distributed to $(2n+1)^2$ neighboring grid points within the square of side $2n$ centered at the point $\boldsymbol{x}'_B = (i_B, j_B)\delta_x$ with the weight W depending on the distance $|\boldsymbol{r}_j - \boldsymbol{x}'_B|$ according to Eq. (9). The "smearing" function $w(x_j, i_B)$ used here is an approximation of what was proposed by Peskin [17]. The effect of the "smearing" range n will be tested in the simulations.

The velocity field $\boldsymbol{u}$ must be evaluated at marker points $\{\boldsymbol{x}_k\}$ from their surrounding Eulerian grid points $\{\boldsymbol{r}_j\}$ by interpolations. One choice is to use Eq. (9) for the force distribution. We can also use a bi-linear interpolation to compute $\boldsymbol{u}(\boldsymbol{x}_k)$ from four nearby grid points or a polynomial stencil based on the nine points of the D2Q9 model (cf. Appendix C in [23]). These interpolations will also be tested in our simulations.

Since an interface is a $(d-1)$ dimensional object in a d dimensional space, the interface-tracking computation would involve a minor fraction of total grid points when the interfacial geometry is not too complicated. In contrast, the interaction force in the multiphase LBE diffusive interface capturing method must be evaluated throughout the entire computational domain. Therefore, the LBE-FT method can be more computationally efficient than the multiphase LBE diffusive interface capturing method. However, a major drawback of the front-tracking method is its difficulty to handle topological changes of interfacial geometry without artificial intervention. It should also be pointed out that, while the LBE-FT method conserves mass globally, it does not conserve mass locally in the interfacial regions where interpolations are applied.

3. Results and discussions

We use the front-tracking LBE method to simulate two simple test cases: (1) a single circular bubble in a flow either quiescent or moving with a constant velocity; and (2) the decay of oscillating capillary wave at the interface between two viscous fluids of equal viscosities and densities. We also compare the proposed LBE-FT method with the existing multiphase LBE diffusive interface capturing method. In what follows we use the units of $\delta_x = \delta_t = 1$ for the sake of convenience. All the quantities, such as the surface tension σ and the viscosity v are given in the "lattice units".

3.1. A circular bubble

For a circular bubble in a quiescent flow, with a given value of the surface tension σ, the pressure difference across the interfacial boundary defined by the circle of radius R satisfies Laplace's law

$$\Delta p = (p_2 - p_1) = \sigma C = c_s^2 \Delta \rho, \quad c_s^2 = \frac{1}{3}, \tag{10}$$

where $C = 1/R$ is the curvature, $p_2 = c_s^2 \rho_2$ and $p_1 = c_s^2 \rho_1$ are the pressures within and without the bubble, $\Delta \rho = (\rho_2 - \rho_1)$ is the density difference across the interface and the ideal gas equation of state for the LBE model has been used.

Using a square mesh of size $N_x \times N_y$ with periodic boundary conditions in both directions, we initialize the system as follows. A circle of radius R is centered at $r_c = (x_c, y_c)$, and there are N marker points evenly distributed on the circumference of the interfacial boundary. The fluid densities inside and outside of the circle are $\rho_2 = 1 + \Delta\rho$ and $\rho_1 = 1$, respectively. After a number of initial iterations, the density equilibrates to a smoothly varying profile across the interface. The thickness of the profile depends on the number of points n used to distribute the capillary force from a marker point x_k to its neighboring grid points $\{r_j\}$: the more points, the thicker the interface.

We first measure the normalized pressure along the radial direction r

$$\bar{p}(r) = \frac{p(r) - p_1}{p_2 - p_1} = \frac{p(r) - p_1}{\Delta p} \in [0, 1].$$

Initially the radius of the bubble is $R_0 = 15.2$ and the number of markers is $N = 120$. The stencil over which the capillary force is distributed has $(2n + 1)^2$ grid points, with $n = 2$ or 3. The system size is $N_x \times N_y = 121 \times 121$. The viscosity $v = 0.001$ and the surface tension $\sigma = 0.022$. The Ohnesorge number $Oh = v/\sqrt{2\rho\sigma R_0}$ is $1/818$, where $\rho = \rho_1 = 1$. The interface profile stabilizes after an initial period of time. The measurement is made after 1000 iterations. As shown in Fig. 3, a larger n leads to a thicker interface. We note that radius of the bubble changes very little in time. For the particular case of Fig. 3, $R \approx 0.9999R_0$ after 1000 iterations, and it is independent of n (we used $n = 2$ and 3 in the test). This shows that the LBE-FT method is remarkably isotropic in spite of the underlying square mesh. We also note that in the LBE front-tracking simulations, the pressures within and without of the interface, p_2 and p_1, steadily maintain their specified initial values, while this is not possible in the LBE diffusive interface capturing schemes. In the LBE capturing schemes with either interaction (e.g. [15]) or free energy (e.g. [16]), the pressures inside and outside of the bubble are difficult to be initialized accurately thus they are constantly changing [28,29]. A comparison of the LBE-FT method and a multiphase LBGK diffusive interface method will be given in Section 3.3.

We further investigate the variations of the radius R and the area $A = 2\pi R$ of the bubble in time. The radius R is measured from the circumference $L = 2\pi R = \sum_k \ell_{kk+1}$ defined by the marker points $\{x_k\}$. We find that, while the bubble remains circular, on average both its radius R and the total area A decrease monotonically but very slowly in time t, as shown in Fig. 4. The system size for the results shown in Fig. 4 is $N_x \times N_y = 131^2$, the initial radius $R_0 = 19.8$, the number of marker points is $N = 155$, the viscosity $v = 0.0035$, and the surface tension $\sigma = 0.04$ ($Oh = 1/360$). With these parameters, the radius R decreases about 0.15% during 10^4 iterations, while the area A decreases about 0.32%, shown as solid lines in Fig. 4. The reason for R and A to vary is that the LBE method only conserves the fluid masses over the entire system, but not the fluid masses or volumes within and without the interface individually. The rates of variation of the bubble radius R and area A depend on the number n, i.e., the way the capillary force is distributed, but independent of the viscosity v. It
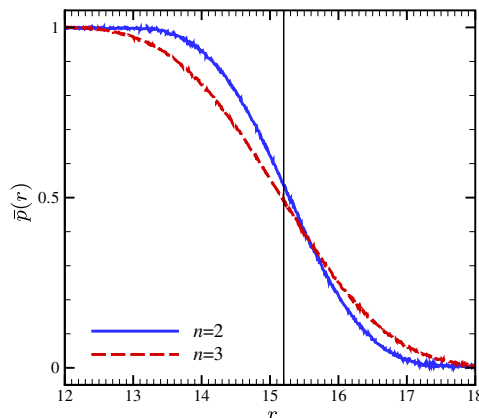

Fig. 3. The normalized pressure $\bar{p}(r)$ across the interface for a bubble in a quiescent flow. The initial radius $R_0 = 15.2$, indicated by the vertical line. The viscosity $v = 0.001$, and the surface tension $\sigma = 0.022$ ($Oh = 0.001223$). The measurements are obtained after 1000 iterations.
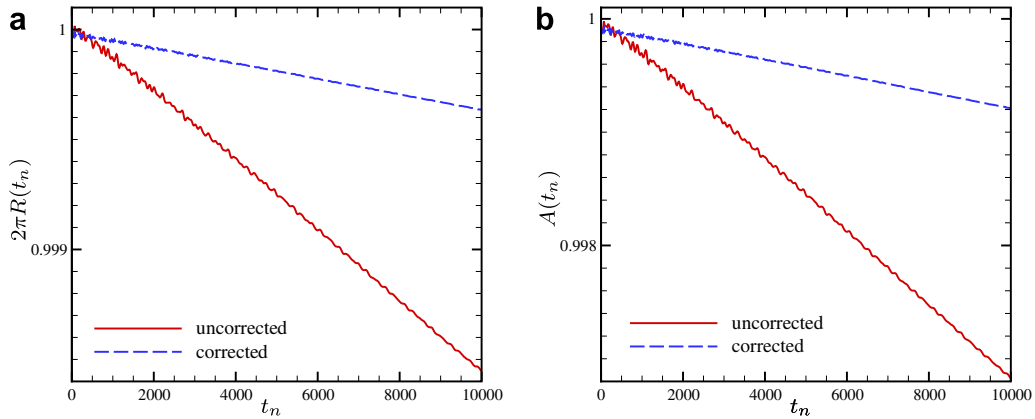
Fig. 4. The time-dependence of (a) the circumference $2\pi R$ and (b) the total area $A = \pi R^2$ of a bubble in quiescent flow. The initial radius $R_0 = 19.8$, $N_x \times N_y = 131^2$, the viscosity $v = 0.0035$, the surface tension $\sigma = 0.04$, and $n = 2$.

should also be noted that the changes in R and A are so little that they are negligible per time step (about $10^{-5}\%$).

The variations in R and A can be reduced by a very simple prediction–correction scheme as the following:

$$f_0^*(t_n) = f_0(t_n) - \vartheta[A(t_n) - A(t_{n-1})], \tag{11}$$

where the parameter $\vartheta > 0$ is determined empirically. The above correction scheme is applied to all nodes within the interface region. Obviously, when the bubble is shrinking, the above correction scheme adds mass (with zero particle velocity) uniformly inside the interface and this increases the pressure p inside the bubble to counter-act the shrinking. With $\vartheta = 4.0$, the variations of R and A are shown as dashed lines in Fig. 4. The rates of change in R and A are reduced by a factor of about 4.0.

Observed in many surface tension simulation methods, spurious currents are vortices in the neighborhood of interfaces despite the absence of any external forcing [30,37], which were first discovered in the lattice Boltzmann method [31]. Spurious currents are due to discretization errors and have been investigated in some recent studies [32–37]. Fig. 5 shows the vector field and the magnitude contour of the spurious current, corresponding to the case of Fig. 4. It is interesting to note that, near the interface, spurious currents are
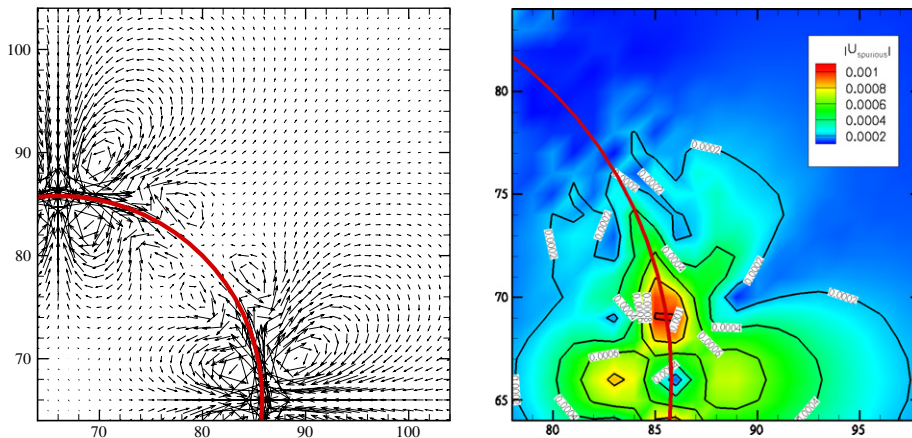

Fig. 5. The spurious velocity field corresponding the simulation of Fig. 4. The (red) solid line indicates the interface location. The magnified spurious velocity vector field (left) and the magnitude contours of spurious velocity (right). The maximum magnitude of the spurious current is $U_{\text{spurious}} \approx 1.02 \times 10^{-3}$. (For interpretation of the references in colour in this figure legend, the reader is referred to the web version of this article.)

tangential to the interface, indicating the absence of radial component of the spurious forcing. This explains why the bubble is rather stable in its size and shape.

Although the amplitude of the spurious currents fluctuates in time, it is observed in other methods that its averaged maximum value scales approximately with the ratio σ/v for large v [37], that is, the capillary number based on the maximum spurious velocity U_{spurious}, $Ca_s := U_{\text{spurious}} v/\sigma$, is a constant. For a bubble of radius 30, the maximum of $Ca_s \simeq 7.0 \times 10^{-5}$, which is smaller than for standard VOF techniques [38] and existing LBE models [39], but not as small as observed in some more sophisticated techniques [37,40]. We find that the amplitude of the spurious currents depends very little on the Ohnesorge number Oh when $0.004 \leqslant Oh \leqslant 0.02$. The spurious currents may be originated from two major sources: the simple "smearing" function and the anisotropy in small scales close to grid spacing. In the grid scale, the LBE model has the spurious invariance of checker-board pattern [21,41], which may affect the spurious current.

If we simulate a bubble in the flow of a uniform velocity, we find similar results as in the quiescent flow. The bubble is indeed advected with the mean flow velocity. Therefore the model is satisfactory in terms of global advection. The residual spurious currents are somewhat smaller than that observed in the quiescent flow.

3.2. Capillary waves

To understand the dynamic behavior of the model, we use the LBE front-tracking scheme to simulate capillary waves between two fluids of equal densities and viscosities. The system is a rectangular domain of size $N_x \times N_y$ with periodic boundary conditions along the x-direction and the no-slip boundary conditions at $y = 1$ and $y = N_y$, which are realized by using the bounce-back schemes. The fluids with uniform density $\rho = 1$ are quiescent initially. The markers $\boldsymbol{x}_i = (x_i, y_i)$ are uniformly distributed on a sinusoidal curve

$$y_i = \frac{1}{2}(1 + N_y) + Y_0 \cos(kx_i), \quad k = 2\pi k_x/N_x, \quad k_x = \text{integer}. \tag{12}$$

The N segments connecting markers are such that they satisfy periodic boundary conditions along x axis.

For given viscosity v, surface tension σ and $k = 2\pi/N_x$, the dimensionless frequency ω_0, the dissipation ε_0, and the Ohnesorge number Oh of the system are

$$\omega_0 = \sqrt{\frac{\sigma k^3}{2\rho}}, \quad \varepsilon_0 = \frac{vk^2}{\omega_0}, \quad Oh = v\sqrt{\frac{\rho}{\sigma N_x}} = \frac{\varepsilon_0}{2\sqrt{\pi}}, \tag{13}$$

where $\rho = 1$. We will conduct simulations with various values of Oh.

We first show in Fig. 6 the evolution of the velocity field $\boldsymbol{u} = (u, v)$ along a vertical cut for the 2D capillary wave. The parameters are: $N_x \times N_y = 151 \times 361$, $v = 0.0045$ and $\sigma = 0.045$. The attenuation rate $\gamma \approx 3.30\times$
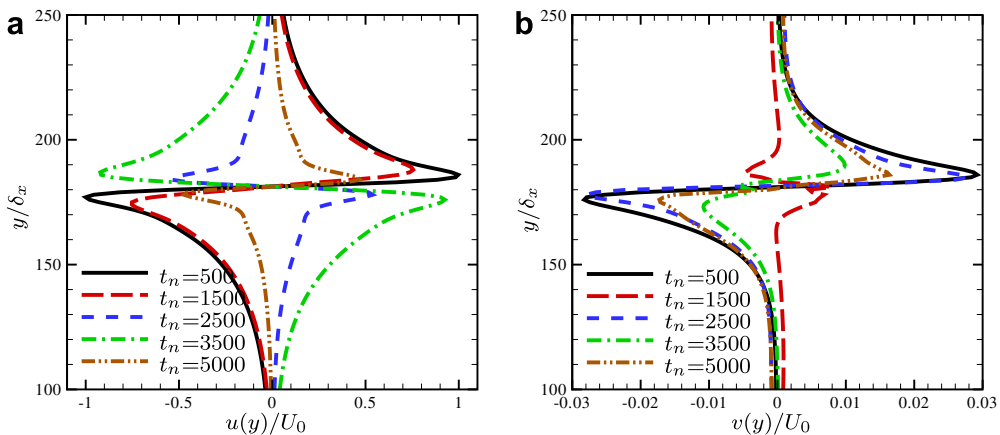

Fig. 6. Evolution of the velocity field. (a) x-component (tangential) velocity $u(y_i)/U_0$ and (b) y-component (perpendicular) velocity $v(y_i)/U_0$, $U_0 \approx 1.237 \times 10^{-3}$. Other parameters are: $N_x \times N_y = 151 \times 361$, $v = 0.0045$ and $\sigma = 0.045$.

10^{-5} and the period $T \approx 5106\delta_t$. We measure the velocity at $x = 3(N_x + 1)/4 = 114$. Figs. 6a and 6b show the dynamics of the tangential velocity $u(y_i)/U_0$ and transverse velocity $v(y_i)/U_0$, respectively, where $U_0 \approx 1.237 \times 10^{-3}c$ is the maximum value of $|u(y_i)|$ at $t = 500\delta_t$. It is clear that the tangential velocity $u(y_i)$ is continuous across the interface.

We next study the dependence of the period T and the attenuation rate γ on the viscosity v and the grid size N_x. We use $N_y = 171$, $k_x = 1$, and $Y_0 = 1.5$ unless otherwise stated. We use a sufficiently large system size to minimize the boundary effect on the oscillation frequency ω and the finite-size effect on the attenuation of the capillary wave. Other parameters used in the following simulations are: the surface tension $\sigma = 0.065$ and the bulk viscosity $\zeta = 0.1$. In principle, the bulk viscosity ζ plays very little role, if any, in the capillary wave phenomenon, we choose a fairly large value ($\zeta = 0.1$) so that the density fluctuations due to inconsistent initial conditions in the simulation can be quickly dissipated. We use $v = 0.0025, 0.0035, 0.0045, 0.0055$ and 0.0065, $N_x = 65, 81, 101, 111, 131$ and 151, and $k = 2\pi/N_x$, corresponding to $0.8 \times 10^{-3} \leqslant Oh \leqslant 3.2 \times 10^{-3}$.

For the force distribution, we use $n = 2$ and 3, unless otherwise stated. Eq. (9) with $n = 2$ is also used to evaluate the velocity field at the marker points from their neighboring Eulerian grid points, and this is equivalent to second-order interpolations.

Starting from a quiescent fluid with markers distributed on the sinusoidal interface defined by Eq. (12), we compute the time evolution of the normalized wave amplitude

$$\bar{y}(t_n) := \frac{1}{\bar{y}_0} \sum_i y_i(t_n) \cos(kx_i), \quad \bar{y}_0 := \sum_i y_i(0) \cos(kx_i). \tag{14}$$

Based on the extended normal mode solutions of surface waves [42–44], the amplitude of the capillary wave evolves as $\cos(\omega t) \exp(-\gamma t)$, where ω is the frequency and γ is the attenuation rate, obtained from the solution of the dispersion equation. Fig. 7 shows the evolution of $\bar{y}(t_n)$ in a typical simulation. The data shown in Fig. 7 is used to compute the period $T = 2\pi/\omega$ and the attenuation rate γ of the capillary wave.

Fig. 8 shows the dependence of the attenuation rate γ and the period T on the viscosity v, with different resolution N_x for one wavelength. The theoretical values of γ and T are obtained by formulas given in [43,44], where the densities and viscosities of fluid I and fluid II are equal. We observe that both the attenuation rate γ and the period T monotonically depend on the viscosity v, although the viscosity dependence of T is very weak. We also observe that the numerical values of γ are always smaller than the theoretical ones, while the numerical values of the period T are always (slightly) larger.

We further study the convergence behavior of γ and T. We compute the absolute ($\Delta\gamma$) and the relative ($\Delta\bar{\gamma}$) errors

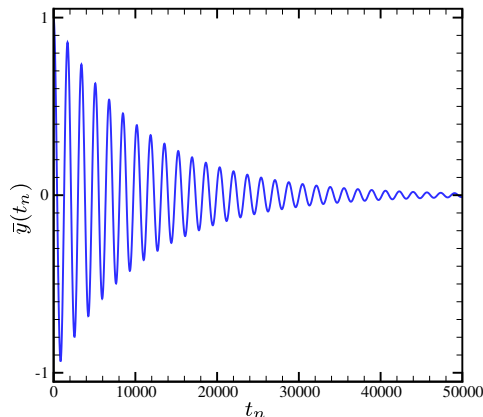$$\Delta\gamma = |\gamma - \gamma_0|, \quad \Delta\bar{\gamma} = \frac{\Delta\gamma}{\gamma_0}, \tag{15}$$

Fig. 7. Evolution of the capillary wave amplitude normalized by its initial value. Parameters are: $N_x = 81$, $k_x = 1$, $Y_0 = 1.5$, $v = 0.045$ and $\sigma = 0.065$.
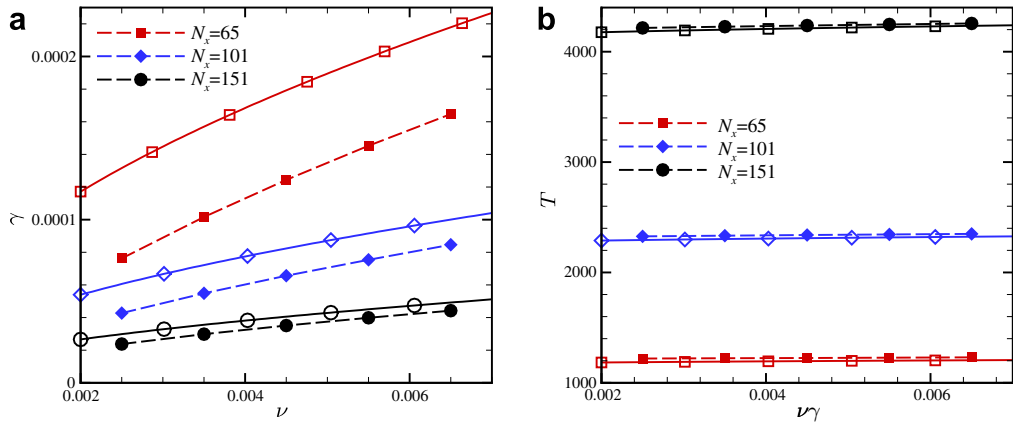
Fig. 8. Dependence of (a) the attenuation rate γ and (b) the period T (right) on the viscosity v and the resolution N_x for one wavelength. $N_y = 171$, $\sigma = 0.065$, and $n = 2$. The solid lines with hollow symbols and dashed lines with solid symbols correspond to theoretical and numerical values, respectively.

where γ_0 is obtained from dispersion relation [43,44]. Fig. 9 shows both the absolute and relative errors of γ, with dependence on the viscosity v and the parameter $n = 2$ and 3. For the attenuation rate γ, the computed rates of convergence are about 2.8 and 1.0 for the absolute and the relative errors, respectively.

Fig. 10 shows the relative error $\Delta\overline{T}$ of the period T

$$\Delta T = |T - T_0|, \quad \Delta\overline{T} = \frac{\Delta T}{T_0}, \tag{16}$$

where T_0 is obtained from the normal-mode analysis [43,44]. The rate of convergence computed from the data is about 1.5.

To further validate the LBE-FT method, we will compare the LBE-FT solution with Prosperetti's initial-value solution for the amplitude of the capillary wave [45] in which we have set that the two fluids on either side of the boundary have the same density and viscosity. For a system of size $N_x \times N_y$, we use $N_y = 1.6N_x$ to ensure that the boundary effect is negligible. The initial conditions are that of a quiescent flow with markers uniformly distributed on the sinusoidal interface defined by Eq. (12), as in the previous tests. The surface tension is fixed at $\sigma = 0.04$. For each run with fixed parameters, we carry out a number of iterations $N_t = 4\pi/\omega_0$.
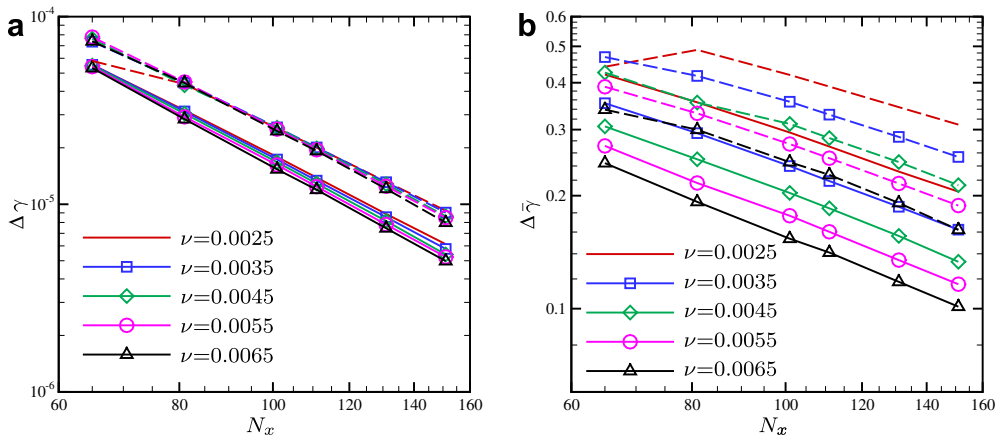

Fig. 9. Convergence of the attenuation rate γ. $N_y = 171$, $\sigma = 0.065$, and $n = 2$ (solid lines) and 3 (dashed lines). The absolute error $\Delta\gamma$ (a) and the relative error $\Delta\overline{\gamma}$ (b) are shown as function of N_x, with different values of v. The solid lines and dashed lines correspond to $n = 2$ and 3, respectively.
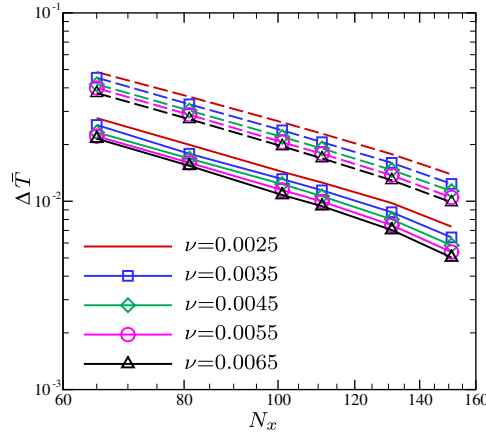
Fig. 10. Convergence of the period T. $N_y = 171$, $\sigma = 0.065$, and $n = 2$ (solid lines) and 3 (dashed lines). The relative error $\Delta\overline{T}$ is shown as a function of N_x with different values of v. The solid lines and dashed lines correspond to $n = 2$ and 3, respectively.

We use the time series of the normalized wave amplitude $\bar{y}(t_n)$ to compute the surface tension σ and the dissipation ε by using the least-square fitting with Prosperetti's solution for the wave amplitude [45]. We then obtain the relative errors of σ and ε depending on the resolution N_x and the dissipation ε_0. We also compute the root-mean-square (RMS) error for the wave amplitude

$$E_2(\bar{y}) := \sqrt{\frac{1}{t_0} \int_0^{t_0} |\bar{y}(t) - \bar{y}^*(t)|^2 \, dt}, \tag{17}$$

where $t_0 = N_t \omega_0 = 4\pi \approx 12.566$ and $\bar{y}^*(t)$ is Prosperetti's solution. Both $\bar{y}(t)$ and $\bar{y}^*(t)$ are so normalized that $\bar{y}(0) = \bar{y}^*(0) = 1$, as indicated in Eq. (14).

Fig. 11 shows the convergence in σ and ε. Clearly, both σ and ε obtained by the LBE-FT method converges to Prosperetti's solution. Also, the convergence in σ and ε is insensitive to the dissipation ε. We show the LBE-FT solution $\bar{y}(t_n)$ for the wave amplitude with $N_x = 48$ and 158 along with Prosperetti's solution $\bar{y}^*(t_n)$ in Fig. 12a. In Fig. 12b we show the RMS error $E_2(\bar{y})$ with several values of ε_0. Clearly, the wave amplitude $\bar{y}$ also converges to Prosperetti's solution, and the rate of convergence seems to be insensitive to the value of ε.

To compare our results with the existing data [33,37], we simulate the capillary wave with $Oh = 1/\sqrt{3000}$. The parameters used the simulations are: the surface tension $\sigma = 0.04$, the time for averaging $t_0 = 8\pi \approx 25.13$, and the "smearing" range $n = 2$ and 3. The interpolations for the velocity field $\boldsymbol{u}$ involve the nine-point stencil
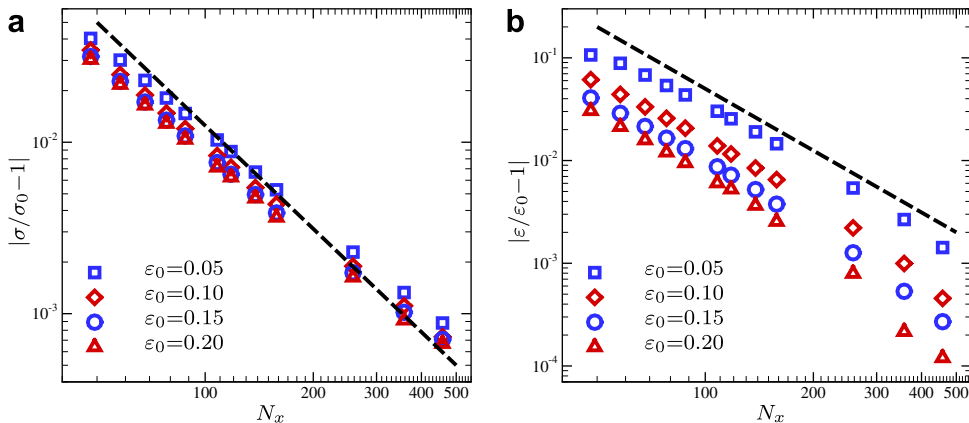

Fig. 11. Convergence of (a) the surface tension σ and (b) the dissipation ε. $\sigma_0 = 0.04$, $n = 2$ for the "smearing" range of the interface force distribution and bi-linear interpolations are used to evaluate the velocity field at marker points. The dashed lines have a slope of -2.
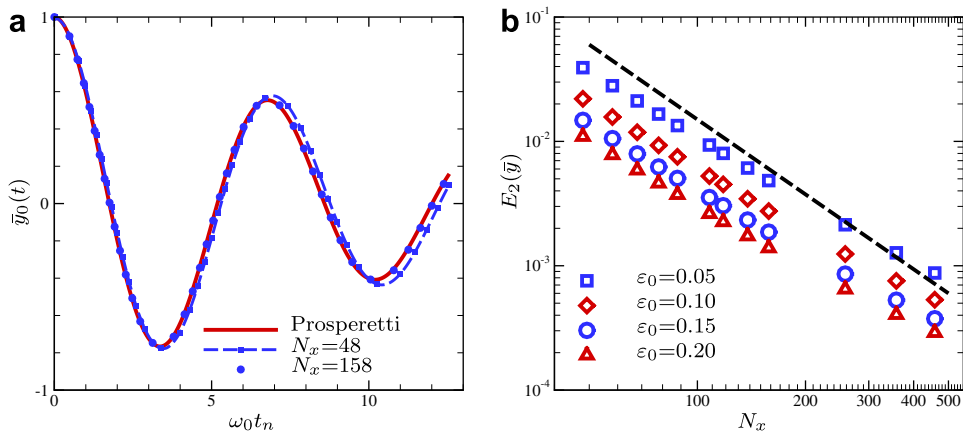
Fig. 12. Convergence of the wave amplitude $\bar{y}(t_n)$. (a) The LBE-FT numerical solutions of $\bar{y}(t_n)$ with $N_x = 48$ and 158 and Prosperetti's solution. (b) Time averaged L_2-norm error $E_2(\bar{y})$. The dashed line has a slope of -2.

based on the D2Q9 model (cf. Appendix C in [23]). We test two types of boundary conditions in the y-direction: the periodic and the free-slip boundary conditions. For the free-slip boundary conditions, particles reverse their momenta normal to the boundary, while maintaining their momenta tangential to the boundary. We use squares of $N_x \times N_y = N_x \times N_x$ and rectangles of $N_x \times N_y = N_x \times 2N_x$ with $N_x = 8$, 16, 32, and 64 as the computational domain. Table 1 compiles the results for the time averaged L_2-normed error of wave amplitude $E_2(\bar{y})$ with respect to Prosperetti's solution. FT and PROST in Table 1 are the results from [33,37], respectively. Our observations are the following. First of all, in all cases the error $E_2(\bar{y})$ has a second-order rate of convergence. Second, the larger the "smearing" range n, the smaller the error. This is true except for some cases of $N_x = 8$. And third, for the free-slip boundary conditions, the error $E_2(\bar{y})$ is systematically decreasing faster with the rectangular domain than the square one as the mesh size increases, while for the periodic boundary conditions, the error with the rectangular domain is slightly larger than that with the square domain. In general, our results agree with the previous ones [33,37].

The above comparisons of the LBE-FT solution with the normal mode solution of the dispersion equation and Prosperetti's initial-value solution [45] lead to the following observation. The numerical results of the period T (or frequency ω), the attenuation rate γ, the surface tension σ and the time-averaged L_2 error of the wave amplitude agree well with the normal mode and Prosperetti's solutions. The values of Oh in this set of simulations are $1.41 \times 10^{-2} \leqslant Oh \leqslant 5.64 \times 10^{-2}$. Note that these values of Oh (more than an order of magnitude larger than for the normal-mode test) were chosen to increase the contribution of transients at small times. Our results of Figs. 11 and 12b clearly indicate that the convergence rate of the LBE-FT method is of second-order. It is interesting to note that the front-tracking with a Navier–Stokes solver [37] did not achieve

Table 1
Convergence of the time averaged L_2-normed error of wave amplitude $E_2(\bar{y})$ with respect to Prosperetti's solution

$N_x \times N_y$	Periodic BCs		Free-slip BCs		VOF	
	$n = 2$	$n = 3$	$n = 2$	$n = 3$	FT	PROST
8×8	0.30108	0.30149	0.29030	0.28927	0.2972	0.2960
16×16	0.08515	0.07920	0.09285	0.08688	0.0778	0.0818
32×32	0.02444	0.02166	0.03075	0.02807	0.0131	0.0069
64×64	0.00818	0.00744	0.01247	0.01173	0.0098	0.0018
8×16	0.28637	0.28651	0.28636	0.28650		
16×32	0.08821	0.08227	0.08823	0.08228		
32×64	0.02656	0.02382	0.02657	0.02383		
64×128	0.00834	0.00751	0.00835	0.00752		

The time average is over $t_0 = 8\pi \approx 25.13$, the surface tension $\sigma = 0.04$, $Oh = 1/\sqrt{3000}$, the dissipation $\varepsilon = 2\sqrt{\pi}Oh = \sqrt{\pi/750}$, and n is the "smearing" range in Eq. (9). FT and PROST are the results from [37,33], respectively.

a second-order rate of convergence. The rate of convergence of the LBE-FT method seems to be insensitive to the "smearing" range of the interface force (we used $n = 2$ and 3 in Eq. (9)) and the order of interpolations to evaluate velocity field on marker points (we use both first- and second-order interpolations).

While Prosperetti's initial-value solution [45] can help to initialize flow fields more accurately for the capillary wave problem (cf. [37]), we ensure that the effect due to inconsistent initial conditions is quickly dissipated, due to the value of ζ chosen here. To estimate the effect due to inconsistent initial conditions, we compare the period T and the attenuation rate γ obtained from both normal-mode [43] and Prosperetti's solutions with the parameters corresponding to our simulations within one period of oscillation. The differences between the results obtained from these two methods are only in the order of 1/1000, for a range of parameters corresponding to $0.0007 \leqslant Oh \leqslant 0.004$. The difference between the two results diminishes rapidly as the interval of time within which the comparison is made increases. Therefore, the systematic error due to inconsistent initial conditions is rather small for the cases studied here. The compressibility in the LBE method may be another source of error pertinent to this test. A systematic error analysis shall be carried in our future study.

3.3. A comparison of MRT-FT and LBGK diffusive interface methods

The proposed LBE front-tracking method differs from the existing multiphase lattice BGK diffusive interface capturing method in several aspects. The density difference in the front-tracking method is maintained mechanically by the surface tension, while in the multiphase LBE method it is due to a non-ideal gas equation of state, which usually does not consider the surface tension explicitly. In the multiphase LBE method, the surface tension is a numerical artifact which is difficult to control independently [28]. In what follows, we will provide a comparison between the proposed LBE-FT method and the existing multiphase LBGK interface capturing schemes.

First of all, the MRT collision model can significantly improve numerical stability (e.g. [46]). With a non-zero mean flow velocity, we can show that the MRT-LBE is more stable than the corresponding LBGK equation. As an example, we use a bubble of radius $10.2\delta_x$ and $\sigma = 0.2$ in a system of size $N_x \times N_y = 519 \times 101$ and with periodic boundary conditions in both directions. The flow is initialized with a uniform velocity $U_x = 0.2c$ along the x-axis. When the viscosity $\nu \leqslant 0.006$, the LBGK equation diverges after a number of iterations, as shown in Table 2, whereas the MRT-LBE is stable in all these cases and beyond. The relaxation rates in the MRT-LBE are: $s_2 = 1.3$, $s_3 = 1.4$, and $s_4 = s_5 = 1.9$. After 2000 iterations, the MRT-LBE yields the result that the bubble has been advected by a distance of about $402\delta_x$ along the x direction, which is about 0.5% off the distance based on the uniform advection velocity U_x. This clearly demonstrates the superiority of the MRT-LBE over the LBGK equation in terms of numerical stability [21].

The most important distinction between front-tracking and diffusive interface capturing is, of course, the treatment of the interface. In the front-tracking method, interfacial locations are tracked by a set of Lagrangian marker points from which the interfacial forces are evaluated, while in the diffusive interface capturing method, interfacial locations are somewhat arbitrarily defined by the contours of some continuous function which has to be computed throughout the entire domain. This has some important ramifications. First of all, the computational efficiency of these two methods is quite different. We will use the single bubble problem as an example. We use a system of size $N_x \times N_y = 191^2$ with a bubble of radius $R_0 = 20\delta_x$ located in the center of the domain. We compare the proposed MRT-FT method with the multiphase lattice BGK method as described in [29], which is an improved version of the interaction model [15]. The multiphase LBGK model [29] uses the van der Waals equation of state: $p_0 = \rho\mu_0 - E_0$, where $\mu_0 = \partial E_0/\partial\rho$ and $E_0 = \rho RT \ln[\rho/(1 - b\rho)] - a\rho^2$, with $a = 9/49$, $b = 2/21$, and $RT = 0.56$. The interface force is given by

$$\boldsymbol{F} = c_s^2 \boldsymbol{\nabla}\rho - \rho\boldsymbol{\nabla}(\mu_0 - \kappa\nabla^2\rho),$$

Table 2
The viscosity dependence of the number of iterations before the LBGK equation diverges for a bubble in a uniform velocity $U_x = 0.2c$

ν	0.0020	0.0040	0.0045	0.0050	0.0055	0.0060
Iterations	1	560	685	890	1165	1565

The surface tension $\sigma = 0.2$ and the bubble radius $R_0 = 10.2\delta_x$, and $0.001 \leqslant Oh \leqslant 0.003$.

where $\kappa = 0.037$ and the gradient ∇ and the Laplacian ∇^2 are discretized with the stencils to reduce spurious currents [29]. With the system size of 191^2, the MRT-FT code is more than 4 times faster than the multiphase LBGK code per time step. The reason is simple. While a bare-bone MRT-LBE code (without front-tracking part) is about 20% slower than the corresponding bare-bone LBGK code, the interface tracking is carried out only in the interface region, which is a small fraction of the entire domain and adds less than 10% in terms of the CPU time in this case. Therefore, the MRT-FT code takes about 30% more CPU time than a bare-bone LBGK code in this case. For the multiphase LBGK method, the interface force has to be computed indiscriminately throughout the entire domain which becomes a significant part of the calculation. This alone leads to the factor of 4 in favor of the MRT-FT method for this particular test case.

The initialization is another problem which deserves our attention. For the MRT-FT method, the surface tension σ and the bubble radius R can be easily specified *a priori* and arbitrarily in a continuous range allowed by the stability of the method. The density profile across interface can develop quickly after a small number of iterations. Because the initial interface density profile cannot be specified exactly, the density relaxation due to inconsistent initial conditions generates acoustic waves in the system, which decay as $e^{-(v/2+\zeta)k^2 t}$, where $k = 2\pi/N_x$. To accelerate this initial density relaxation, we can use the absorbing boundary conditions instead of the periodic boundary conditions, which simply make the distribution functions $\{f_i\}$ entering the computational domain equal at the last two adjacent lines at the boundaries, i.e.,

$$f_i(N_x, y_j) = f_i(N_x - 1, y_j), \quad f_i(1, y_j) = f_i(2, y_j) \ \forall y_j, \ \boldsymbol{c}_i \cdot \hat{\boldsymbol{n}} < 0,$$
$$f_i(x_i, N_y) = f_i(x_i, N_y - 1), \quad f_i(x_i, 1) = f_i(x_i, 2) \ \forall x_i, \ \boldsymbol{c}_i \cdot \hat{\boldsymbol{n}} < 0,$$

where $\hat{\boldsymbol{n}}$ is the unit vector out-normal to the boundaries. The absorbing boundary conditions can quickly dissipate the acoustic waves due to the inaccurate initial conditions, as shown in Fig. 13a.

In Fig. 13a we show the time series of the following normalized pressure difference

$$\delta\bar{p} := (\bar{p}_1 - \bar{p}_2)R_0/\sigma_0,$$

where $\bar{p}_1$ is the pressure averaged over a co-centric disc of radius $r \leqslant 10\delta_x$ inside the bubble and r is the distance to the bubble center, $\bar{p}_2$ is averaged over a co-centric ring of $30\delta_x \leqslant r \leqslant 40\delta_x$ outside of the bubble, and R_0 and σ_0 are the initial bubble radius and surface tension, respectively. If the MRT-FT method is consistent with Laplace's law with the given R_0 and σ_0, then $\delta\bar{p}$ should converges to unity after the initial relaxation and this is indeed the case. The magnitude of the acoustic waves generated by the initial layer is less than 1% after a few iterations. With the absorbing boundary conditions, it completely disappears after about 200 iterations. We also compute $\delta\bar{p}$ for the multiphase LBGK method with an estimated $\sigma_0 \approx 0.041$ based on $R_0 = 20\delta_x$. Because the multiphase LBGK method has a much thicker interface region, $\bar{p}_2$ is averaged over a co-centric ring
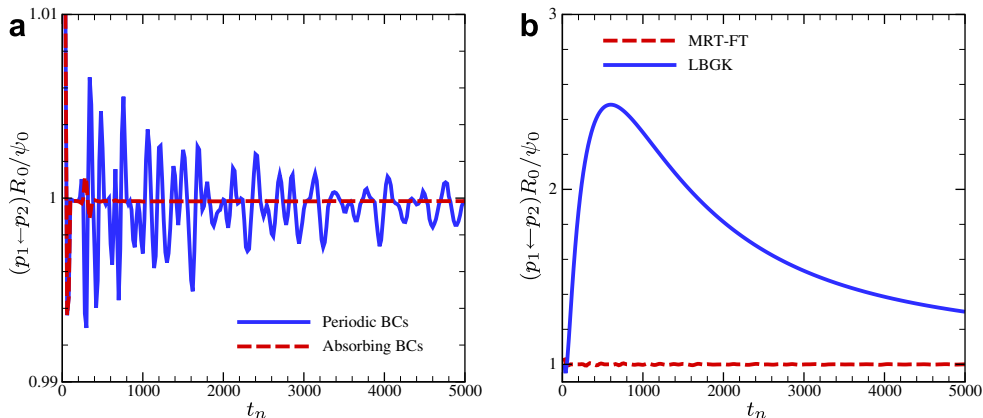

Fig. 13. Normalized pressure fluctuation due to inconsistent initial conditions for a single bubble of $R = 20\delta_x$ and $v = 0.1$. (a) MRT-FT, $s_2 = 1.1$, $s_3 = 1.4$, $s_5 = s_7 = 1.9$, and $\sigma_0 = 0.07$. With absorbing BCs (dashed line), the acoustic waves are damped out faster than the periodic BCs (solid line). (b) The multiphase LBGK diffusive interface capture method (solid line) [29] *vs.* the MRT-FT method (dashed line) with periodic BCs.

of $50\delta_x \leqslant r \leqslant 60\delta_x$, which is sufficiently away from the interface region. The results are shown in Fig. 13b along with the MRT-FT result with the periodic boundary conditions. Obviously, the multiphase LBGK result has not reached the final steady state after 5000 iterations. A conservative estimate indicates that it would take about 10^6 iterations for the multiphase LBGK result to converge [29], while the MRT-FT result converges after less than 10^4 iterations with the periodic boundary conditions. Thus, in terms of the number of iterations to achieve the steady state, there is at least two orders of magnitude difference between the MRT-FT method and the multiphase LBGK method for this simple test.

We next show the normalized density profiles of the two methods in Fig. 14

$$\bar{\rho}(r) = \frac{\rho(r) - \rho_1}{\rho_2 - \rho_1}, \tag{18}$$

where ρ_2 and ρ_1 are the densities inside and outside to the bubble, respectively. Fig. 14 shows the density profiles across the interface region along the x-axis after 5000 iterations. For the MRT-FT method, the interface region covers precisely 5 grid point, that is, the interface thickness is $4\delta_x$, determined by $n = 2$ in the interface forcing "smearing" function of Eq. (9). The interface location varies in the order of $10^{-5}\%$ per time step (cf. Fig. 4 and the related discussions). In contrast, for the multiphase LBGK method [29], the interface thickness is about $15\delta_x$. Because the interface position in the multiphase LBGK method has to be determined from the contours of the density $\bar{\rho}(r)$, the precision of determining the interface position would largely depend on the numerical procedure used. Given the fact that the interface thickness is about $15\delta_x$, which is comparable to the bubble radius $R_0 = 20\delta_x$, one cannot expect to determine the bubble radius to such a precision comparable to what the MRT-FT method can do, i.e., smaller than $10^{-5}\delta_x$ per time step. As an alternative, we determine the variation of the bubble radius as follows. Based on Laplace's law, we compute $\overline{R}(t) = [\bar{p}_2(t) - \bar{p}_1(t)]\sigma_0$ and its relative variation with respect to time t, which is about $5.2 \times 10^{-3}\%$ per time step after 5000 iterations—more than two orders of magnitude larger than that observed in the MRT-FT results. We have also tested the original multiphase LBGK scheme [15], which has a thicker interface region of about $17\delta_x$ and cannot sustain a bubble of $R = 20\delta_x$ with a system of size 191^2. The smallest bubble we can obtained with the original Shan–Chen multiphase LBGK scheme [15] is about $R \approx 67\delta_x$.

The comparison we have shown above leads to the following observations. The proposed MRT-FT method is superior to the existing multiphase LBGK diffusive interface capturing method in three aspects: accuracy of interface representation, numerical stability, and computational efficiency. If the BGK collision model is replaced by the MRT one in the LBE diffusive interface capturing method, the numerical stability can be significantly improved (e.g. [46]). However, the MRT collision model alone would not improve the accuracy of interface representation and computational efficiency of the multiphase LBE diffusive interface capturing method, which are determined by the inherent properties of the diffusive interface method. It should also be emphasized that all the advantages of the MRT-FT method are achieved without sacrificing the simplicity
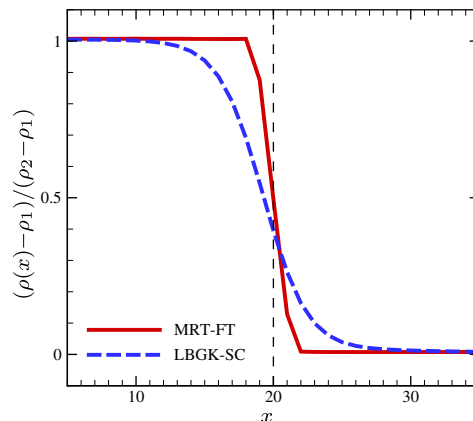

Fig. 14. Normalized density profile across the interface. The MRT-FT (solid line) *vs.* the multiphase LBGK diffusive interface method (dashed line). The profiles correspond to the results of Fig. 13 after 5000 iterations.

of the lattice Boltzmann method, provided that interface geometry is trackable. In addition, the LBE-FT method with MRT collision model has the freedom to independently adjust the surface tension, the transport coefficients and the speed of sound, which is denied to the lattice BGK models.

4. Conclusions

In this work we demonstrate the feasibility of combining the lattice Boltzmann equation for flows and front-tracking technique for modeling and simulation of interfacial dynamics with surface tension in two dimensions. The proposed LBE-FT method is verified by the simulations of a single bubble in quiescent or moving flows and the oscillating capillary wave between the interface of two fluids of equal viscosities and densities. For the single bubble simulations, we measure the spurious currents in the interface region and find the strength of spurious currents is weaker than that found in the standard VOF method and existing LBE models for multiphase fluids. For the capillary wave simulations, we observe that the period T (or the frequency ω), the dissipation rate γ or ε, the surface tension σ and the RMS error of the wave amplitude all agree well with the normal-mode and Prosperetti's solutions, and the convergence rate of the LBE-FT method is of second order, which is difficult to achieve some the conventional front-tracking methods [37].

The proposed LBE-FT method maintains the simplicity of the LBE method. In addition, it has several advantages over the existing multiphase LBE diffusive interface method. First, because of the front-tracking method, the interface location is precisely represented. This is the distinctive feature of the front-tracking method as opposed to diffusive interface methods. The interface for the LBE-FT method is much thinner than what is observed in the multiphase LBE diffusive interface method. Second, the proposed LBE-FT method uses the LBE with multiple-relaxation-times (MRT), therefore it is more stable than the existing lattice BGK method [21,39]. Third, the LBE-FT method is much more computationally efficient than the multiphase LBGK diffusive interface method. Fourth, the strength of the spurious currents observed in the LBE-FT simulations is much weaker than that observed in the existing multiphase LBE models, although we note that the spurious currents can be reduced by other means, such as including more discrete velocities [35], using a difference equation of state [36] or a consistent discretization of the interaction [29]. Fifth, the LBE-FT method can maintain the density difference that varies very slowly in time, which is much more difficult to attain for the existing multiphase LBE method [28,39]. And sixth, the surface tension and other transport coefficient are independently adjustable parameters in the MRT-LBE model, whereas it is not possible for some LBGK models (e.g. [15,16]) to decouple the surface tension from the viscous effect.

We note that the LBE-FT method can be readily extended to 3D, the main difficulty in 3D being the triangulation to represent the interface [7,8]. The "smearing" function to distribute the localized capillary forces can also be easily extended to 3D. Our further research activity will include investigations of the cause of spurious currents and effective and efficient ways to reduce or eliminate them, incorporation of matured and sophisticated numerical techniques, such as the multigrid or implicit time stepping method, into the LBE method. A flow-dependent viscosity in the spirit of LES is also under consideration. These techniques will help to increase the density difference across interfaces, for example.

References

[1] S.J. Osher, G. Tryggvason (Eds.), J. Comput. Phys. Numer. Meth. Multiphase Flows 169 (2) (2001) 249–762 (Special Issue).
[2] S.O. Unverdi, G. Tryggvason, A front-tracking method for viscous, incompressible, multi-fluid flows, J. Comput. Phys. 100 (1) (1992) 25–37.
[3] S.O. Unverdi, G. Tryggvason, Computations of multi-fluid flows, Physica D 60 (1992) 70–83.

[4] G. Tryggvason, B. Bunner, O. Ebrat, W. Tauber, Computations of multiphase flows by a finite difference/front tracking method. I. Multi-fluid flows, in: VKI Lecture Series, vol. 1998–03, The von Karman Institute for Fluid Dynamics, Rhode-St-Genèse, Belgium, 1998.

[5] G. Tryggvason, A. Esmaeeli, S. Mortazavi, J. Han, S. Homma, Computations of multiphase flows by a finite difference/front tracking method. II. Applications, in: VKI Lecture Series, vol. 1998–03, The von Karman Institute for Fluid Dynamics, Rhode-St-Genèse, Belgium, 1998.

[6] G. Tryggvason, D. Juric, J. Che, M.R.H. Nobari, S. Nas, Computations of multiphase flows by a finite difference/front tracking method. III. Variable surface tension and phase change, in: VKI Lecture Series, vol. 1998–03. The von Karman Institute for Fluid Dynamics, Rhode-St-Genèse, Belgium, 1998.

[7] G. Tryggvason, B. Bunner, A. Esmaeeli, N. Al-Rawahi, Computations of multiphase flows, Adv. Appl. Mech. 39 (2003) 81–120.

[8] J. Du, B. Fix, J. Glimm, X. Jia, X. Li, Y. Li, L. Wu, A simple package for front tracking, J. Comput. Phys. 213 (2) (2006) 613–628.

[9] W.J. Rider, D.B. Kothe, Reconstructing volume tracking, J. Comput. Phys. 141 (1997) 112–152.

[10] G.R. McNamara, G. Zanetti, Use of the Boltzmann equation to simulate lattice-gas automata, Phys. Rev. Lett. 61 (20) (1988) 2332–2335.

[11] F.J. Higuera, J. Jiménez, Boltzmann approach to lattice gas simulations, Europhys. Lett. 9 (1989) 663–668.

[12] D. Yu, R. Mei, L.-S. Luo, W. Shyy, Viscous flow computations with the method of lattice Boltzmann equation, Prog. Aerosp. Sci. 39 (2003) 329–367.

[13] M. Sussman, A second order coupled level set and volume-of-fluid method for computing growth and collapse of vapor bubbles, J. Comput. Phys. 187 (2003) 110–136.

[14] E. Aulisa, S. Manservisi, R. Scardovelli, A surface marker algorithm coupled to an area-preserving marker redistribution method for three-dimensional interface tracking, J. Comput. Phys. 197 (2004) 555–584.

[15] X. Shan, H. Chen, Lattice Boltzmann model for simulating flows with multiple phases and components, Phys. Rev. E 47 (3) (1993) 1815–1819.

[16] M.R. Swift, E. Orlandini, W.R. Osborn, J.M. Yeomans, Lattice Boltzmann simulations of liquid–gas and binary fluid systems, Phys. Rev. E 54 (5) (1996) 5041–5052.

[17] C.S. Peskin, Numerical analysis of blood flow in the heart, J. Comput. Phys. 25 (3) (1977) 220–252.

[18] C.S. Peskin, The immersed boundary method, Acta Numer. 11 (2002) 479–517.

[19] Z. Feng, E. Michaelides, Proteus: A direct forcing method in the simulations of particulate flows, J. Comput. Phys. 202 (2005) 20–51.

[20] D. d'Humières, Generalized lattice-Boltzmann equations, in: B.D. Shizgal, D.P. Weave (Eds.), Rarefied Gas Dynamics: Theory and Simulations, Prog. Astronaut. Aeronaut., vol. 159, AIAA, Washington, DC, 1992, pp. 450–458.

[21] P. Lallemand, L.-S. Luo, Theory of the lattice Boltzmann method: dispersion, dissipation, isotropy, Galilean invariance, and stability, Phys. Rev. E 61 (6) (2000) 6546–6562.

[22] D. d'Humières, I. Ginzburg, M. Krafczyk, P. Lallemand, L.-S. Luo, Multiple-relaxation-time lattice Boltzmann models in three dimensions, Philos. Trans. R. Soc. Lond. A 360 (2002) 437–451.

[23] P. Lallemand, L.-S. Luo, Theory of the lattice Boltzmann method: acoustic and thermal properties in two and three dimensions, Phys. Rev. E 68 (2003) 036706.

[24] X. He, L.-S. Luo, Lattice Boltzmann model for the incompressible Navier–Stokes equation, J. Stat. Phys. 88 (1997) 927–944.

[25] I. Ginzbourg, P.M. Adler, Boundary flow condition analysis for the three-dimensional lattice Boltzmann model, J. Phys. II 4 (1994) 191–214.

[26] A.J.C. Ladd, R. Verberg, Lattice-Boltzmann simulation of particle-fluid suspensions, J. Stat. Phys. 104 (2001) 1191–1251.

[27] M. Junk, A. Klar, L.-S. Luo, Asymptotic analysis of the lattice Boltzmann equation, Asymptotic Anal. 210 (2) (2005) 676–704.

[28] X. He, G. Doolen, Thermodynamic foundations of kinetic theory and lattice Boltzmann models for multiphase flows, J. Stat. Phys. 107 (1–2) (2002) 309–328.

[29] T. Lee, P.F. Fisher, Eliminating parasitic currents in the lattice Boltzmann equation method for nonideal gases, Phys. Rev. E 74 (2006) 046709.

[30] R. Scardovelli, S. Zaleski, Direct numerical simulation of free surface and interfacial flow, Annu. Rev. Fluid Mech. 31 (1999) 567–603.

[31] A.K. Gunstensen, Lattice-Boltzmann studies of multiphase flow through porous media, Ph.D. thesis, M.I.T., 1992.

[32] S. Shin, S.I. Abdel-Khalik, V. Daru, D. Juric, Accurate representation of surface tension using the level contour reconstruction method, J. Comput. Phys. 203 (2) (2005) 493–516.

[33] D. Gerlach, G. Tomar, G. Biswas, F. Durst, Comparison of volume-of-fluid methods for surface tension-dominant two-phase flows, Int. J. Heat Mass Trans. 49 (2006) 740–754.

[34] M.M. Francois, S.J. Cummins, E.D. Dendy, D.B. Kothe, J.M. Sicilian, M.W. Williams, A balanced-force algorithm for continuous and sharp interfacial surface tension models within a volume tracking framework, J. Comput. Phys. 213 (2006) 141–173.

[35] X. Shan, Analysis and reduction of the spurious current in a class of multiphase lattice boltzmann models, Phys. Rev. E 73 (2006) 047701.

[36] P. Yuan, L. Schaefer, Equations of state in a lattice Boltzmann model, Phys. Rev. E 73 (2006) 047701.

[37] S. Popinet, S. Zaleski, A front-tracking algorithm for accurate representation of surface tension, Int. J. Numer. Meth. Fluids 30 (1999) 775–793.

[38] B. Lafaurie, C. Nardone, R. Scardovelli, S. Zaleski, G. Zanetti, Modelling merging and fragmentation in multiphase flows with SURFER, J. Comput. Phys. 113 (1994) 134–147.

[39] S. Hou, X. Shan, Q. Zou, G.D. Doolen, W.E. Soll, Evaluation of two lattice Boltzmann models for multiphase flows, J. Comput. Phys. 138 (2) (1997) 695–713.

[40] Y. Renardy, M. Renardy, PROST: A parabolic reconstruction of surface tension for the volume-of-fluid method, J. Comput. Phys. 183 (2002) 400–421.

[41] G.L. Zanetti, Hydrodynamics of lattice-gas automata, Phys. Rev. A 40 (3) (1989) 1539–1548.

[42] H. Lamb, Hydrodynamics, sixth ed., Dover, New York, NY, 1945.

[43] M. Papoular, Ondes de surface dans un système de deux phases fluides superposées, J. Phys. 29 (1) (1968) 81–87.

[44] J. Meunier, Diffusion de la lumière par les ondes de surface sur CO_2 près du point critique. Mesure de la tension superficielle, J. Phys. 30 (11/12) (1969) 933–942.

[45] A. Prosperetti, Free oscillations of drops and bubbles: the initial-value problem, J. Fluid Mech. 100 (1980) 333–347.

[46] K.N. Premnath, J. Abraham, Simulations of binary drop collisions with a multiple-relaxation-time lattice-Boltzmann model, Phys. Fluids 17 (12) (2005) 122105.